

PAPER

The effects of tine coupling and geometrical imperfections on the response of DETF resonators

To cite this article: K Azgin and L Valdevit 2013 *J. Micromech. Microeng.* **23** 125011

View the [article online](#) for updates and enhancements.

Related content

- [MEMS resonant load cells for micro-mechanical test frames](#)
A Torrents, K Azgin, S W Godfrey et al.
- [Nonlinear dynamics of nanomechanical beam resonators: improving the performance of NEMS-based sensors](#)
N Kacem, S Hentz, D Pinto et al.
- [A high-sensitivity biaxial resonant accelerometer with two-stage microleverage mechanisms](#)
Hong Ding, Jiuxuan Zhao, Bing-Feng Ju et al.

Recent citations

- [Sedat Pala et al](#)
- [Design and fabrication of a high performance resonant MEMS temperature sensor](#)
Talha Kose et al
- [A MEMS square Chladni plate resonator](#)
Sedat Pala and Kvanç Azgin

The effects of tine coupling and geometrical imperfections on the response of DETF resonators

K Azgin¹ and L Valdevit^{2,3}

¹ Mechanical Engineering Department, Middle East Technical University, Ankara, Turkey

² Mechanical and Aerospace Engineering Department, University of California, Irvine, CA, USA

E-mail: valdevit@uci.edu

Received 19 May 2013, in final form 6 September 2013

Published 30 October 2013

Online at stacks.iop.org/JMM/23/125011

Abstract

This paper presents a two-degree-of-freedom analytical model for the electromechanical response of double ended tuning fork (DETF) force sensors. The model describes the mechanical interaction between the tines and allows investigation of the effect of a number of asymmetries, in tine stiffness, mass, electromechanical parameters and load sharing between the tines. These asymmetries are introduced during fabrication (e.g., as a result of undercut) and are impossible to completely eliminate in a practical design. The mechanical coupling between the tines induces a frequency separation between the in-phase and the out-of-phase resonant modes. The magnitude of this separation and the relative intensity of the two modes are affected by all the asymmetries mentioned above. Two key conclusions emerge: (i) as the external axial compressive load is increased, the in-phase mode reaches zero frequency (buckling) much faster than the out-of-phase (i.e., operational) mode, resulting in a device with a decreased load range. (ii) During the operation, balanced excitation is essential to guarantee that the out-of-phase mode remain significantly stronger than the in-phase mode, thus allowing sharp phase locked loop locking and hence robust performance. The proposed model can be used to assess the magnitude of asymmetries introduced by a given manufacturing process and accurately predict the performance of DETF force sensors. For the specific sensor characterized in this study, the proposed model can capture the full dynamic response of the DETF and accurately predict its maximum axial compressive load; by contrast, the conventional single-DOF model does not capture peak splitting and overpredicts the maximum load by $\sim 18\%$. The proposed model fits the measured frequency response of the electromechanical system and its load-frequency data with coefficient of determination (R^2) of 95.4% (0.954) and 99.2% (0.992), respectively.

(Some figures may appear in colour only in the online journal)

1. Introduction

Double ended tuning forks (DETF) are a unique class of force sensors, providing high stability, a high dynamic range, low mechanical compliance and easily digitizable output signals. These features make them ideal for the development of highly versatile and ultra-sensitive micro-mechanical load cells for the characterization of complex materials (in particular

micro-architected materials) at the micron-millimeter scale [1]. The DETF structure is composed of two nominally identical suspended parallel tines connected at both ends. In a typical sensor design, one end is clamped to a nominally rigid structure, with the external axial load (tensile or compressive) applied at the opposite end. Upon external axial force application (compressive or tensile), the resonant frequency of the tines changes (decreases or increases, respectively), and this change is detected at the capacitive plates connected with the tines (e.g., by means of a phase locked loop

³ Author to whom any correspondence should be addressed.

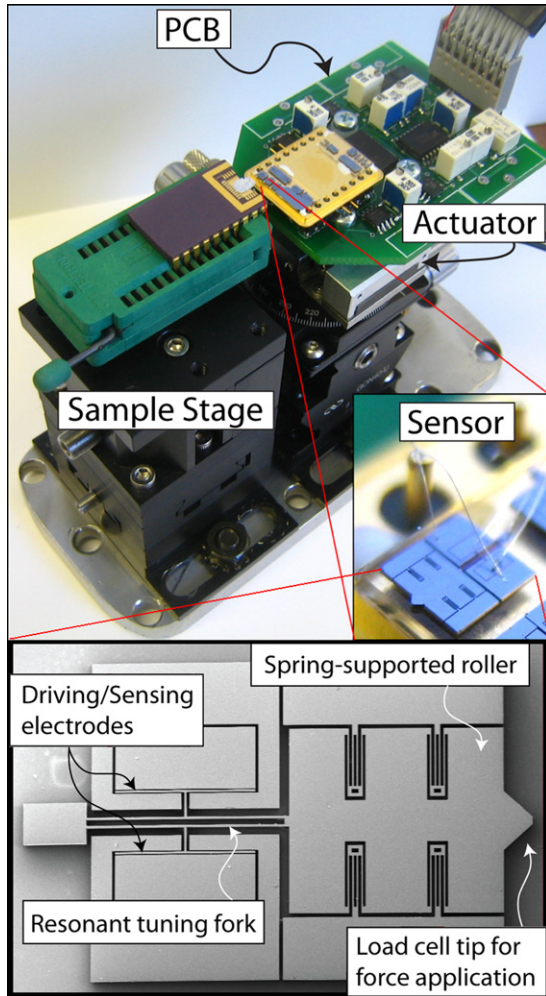


Figure 1. MEMS DETF sensor (SEM image and setup implementation).

(PLL) circuit) and accurately measured with a high-stability frequency counter. Either through modeling or calibration (or a combination thereof), the frequency change can be readily related to the applied force [2–6].

The authors have recently designed, optimized and implemented such a force sensor [7–9] (figure 1), experimentally demonstrating a force resolution of ~ 10 nN and a force range of ~ 0.1 N (in compression). To date, most analytical predictions of the DETF electromechanical response have been based on simple one-degree-of-freedom lumped models [8, 10, 11], which ignore the mechanical interaction between the tines. Although in a perfectly symmetric system with rigid boundaries, the tines are indeed mechanically decoupled, in practice, a finite substrate compliance and any slight imbalance in the geometric parameters and/or materials properties of the tines induce a coupling effect, which affects the sensor response; in essence, load is no longer distributed equally on the two tines, resulting in a non-symmetric vibration pattern of the tine pair. These asymmetries are induced by manufacturing imperfections and are impossible to eliminate completely (or even accurately predict). Undercut is a key example, as it can affect the two tines by slightly different amounts, depending on the device

design. Recent work demonstrated that a robust operation is possible even without accounting for these phenomena in the design process; nonetheless, decoupled models grossly overestimate the buckling load of the tines (by as much as 18%), and hence the sensor range under compressive loads [8]. As the desired force range is often a critical sensor parameter, greatly affecting the DETF design [9], its accurate estimation is critical for the fabrication of robust sensors. Furthermore, an electromechanical model that fully accounts for tine coupling is needed to quantify the effect of various imperfections on the sensor response. This paper describes the development of such a model, and is organized as follows: section 2 describes the analytical model, reviewing the single-degree-of-freedom (1-DOF) approach first and then discussing its extension to two-degrees-of-freedom (2-DOF) systems. In section 3, the new 2-DOF model is exercised to quantify the sensitivity of the resonator response on geometric and materials uncertainties. Experimental verifications are provided in section 4. Conclusions follow.

2. Electro-mechanical modeling

2.1. A 1-DOF electromechanical lumped model

The traditional analysis of DETF resonators ignores dynamic coupling between the two tines and treats each as an independent oscillator, for which a 1-DOF lumped spring–mass model is readily established [8, 10, 11]. This section quickly reviews the formulation.

With reference to figure 2, the dynamic response of the tine in the absence of dissipative phenomena (e.g., damping) is governed by the momentum equation [12]:

$$\frac{\partial^2}{\partial x^2} \left(EI \frac{\partial^2 v(x, t)}{\partial x^2} \right) + \frac{\partial}{\partial x} \left(\frac{F_{\text{appl}}}{2} \frac{\partial v(x, t)}{\partial x} \right) + \rho A \frac{\partial^2 v(x, t)}{\partial t^2} = P_e(x, t) \quad (1)$$

where v is the deflection in the y direction, EI is the flexural stiffness of the tine for bending in the (x, y) plane, F_{appl} is the external axial force on the load cell (equal to twice the force applied on each tine), ρ the materials mass density, A the cross-sectional area of the tine and P_e the transverse actuation force. For the design depicted in figure 1, P_e is a concentrated force at the middle point of the tine (whereas it would be a distributed force along the tine length for driving without actuation plates).

If we assume that a solution can be found by separation of variables, i.e.:

$$v(x, t) = \phi(\varepsilon)y(t) \quad (2)$$

with $\varepsilon = x/L_f$, the solution can be written as [10]:

$$M_{\text{eff}}\ddot{y} + c\dot{y} + K_{\text{eff}}y = P_e(t) \quad (3)$$

where the effective mass, M_{eff} , the effective stiffness, K_{eff} and the damping coefficient c (introduced to model mechanical dissipation) are defined as:

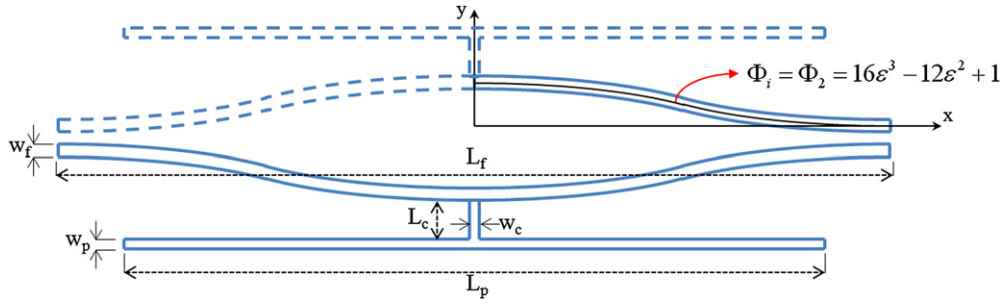


Figure 2. The reference system, geometric variables and assumed mode shape throughout the analysis.

$$K_{\text{eff}} = 2 \frac{EI}{L_f^3} \int_0^{1/2} \left(\frac{d^2 \phi_i}{d\epsilon^2} \right)^2 d\epsilon + 2 \frac{F_{\text{appl}}/2}{L_f} \int_0^{1/2} \left(\frac{d\phi_i}{d\epsilon} \right)^2 d\epsilon$$

$$M_{\text{eff}} = 2\rho AL_f \int_0^{1/2} \phi_i^2 d\epsilon + \sum_j m_j (\phi_i(\epsilon_j))^2$$

$$c = \frac{\sqrt{K_{\text{eff}} M_{\text{eff}}}}{Q} \quad (4)$$

with $\phi_i(\epsilon)$ the vibration mode, m_j the mass of the actuation plate (modeled as a lumped mass), L_f the length of the tine and Q the quality factor of the mechanical oscillator. Approximating the mode shape to the elastica of a clamped-clamped beam subjected to a point load at its center, i.e.,

$$\phi_i = \phi_2 = 16\epsilon^3 - 12\epsilon^2 + 1 \quad (5)$$

the stiffness and mass can be evaluated as:

$$K_{\text{eff}} = 192 \frac{EI}{L_f^3} + 2.4 \frac{F_{\text{appl}}}{L_f}$$

$$M_{\text{eff}} = \frac{13}{35} \rho h w_f L_f + \rho h (w_p L_p + w_c L_c) \quad (6)$$

with L_f, w_f, L_p, w_p, L_c and w_c the length and width of the tine, the actuation plate and the connector, respectively (see figure 2), and h the device thickness. The damped natural frequency of this mode is then:

$$\omega_{n,D} = \sqrt{\frac{K_{\text{eff}}}{M_{\text{eff}}} (1 - 2\xi^2)}$$

$$= \sqrt{\frac{192 \frac{EI}{L_f^3} + 2.4 \frac{F_{\text{appl}}}{L_f}}{\rho h \left(\frac{13}{35} w_f L_f + w_p L_p + w_c L_c \right)}} (1 - 2\xi^2) \quad (7)$$

where ξ is an alternative measure of the damping coefficient, defined as:

$$\xi = \frac{1}{2Q}. \quad (8)$$

Operation of the DETF requires a continuous oscillation of the tines at the frequency of the operational mode. If the tine is forced with a combination of V_{dc} and V_{ac} at a frequency ω as shown schematically in figure 3, the net force on the tine (accounting for both the drive and sense plates) is:

$$P_e(t) = \frac{1}{2} \frac{\epsilon_0 h L_p}{(g-y)^2} (V_{\text{dc}}^2 + V_{\text{ac}}^2 - 2V_{\text{dc}} V_{\text{ac}} \cos(\omega t))$$

$$- \frac{1}{2} \alpha \frac{\epsilon_0 h L_p}{(g+y)^2} V_{\text{dc}}^2 \quad (9)$$

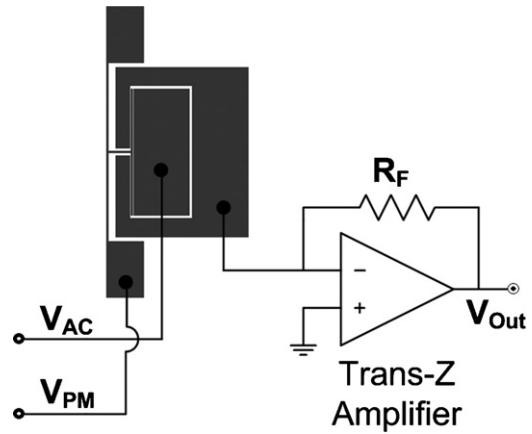


Figure 3. Basic actuation and detection scheme used for resonant excitation.

where g is the initial gap between the actuation plate and the fixed electrode, $y(t)$ the tine displacement and α is the sense-to-drive side ratio of plate-electrode overlap area (generally $\alpha \approx 1$). For very small V_{ac} ($V_{\text{ac}} \ll V_{\text{dc}}$) and for small lateral displacements of the tine during actuation ($y \ll g$), this force reduces to:

$$P_e(t) = \frac{1}{2} \frac{\epsilon_0 h L_p}{g^2} (V_{\text{dc}}^2 (1 - \alpha) - 2V_{\text{dc}} V_{\text{ac}} \cos(\omega t)) \quad (10)$$

whereas the effective stiffness in the lumped equation of motion (equation (3)) becomes:

$$K_{\text{eff},e} = 192 \frac{EI}{L_f^3} + 2.4 \frac{F_{\text{appl}}}{L_f} - \frac{\epsilon_0 h L_p}{g^3} V_{\text{dc}}^2 (1 + \alpha) \quad (11)$$

(In equation (0.11) the term proportional to V_{ac} has been ignored by virtue of $V_{\text{ac}} \ll V_{\text{dc}}$.) The equation of motion can then be written as:

$$\ddot{y}(t) + \frac{\omega_{n,e}}{Q} \dot{y}(t) + \omega_{n,e}^2 y(t) = \frac{1}{2} \frac{\epsilon_0 h L_p}{M_{\text{eff}} g^2}$$

$$\times (V_{\text{dc}}^2 (1 - \alpha) - 2V_{\text{dc}} V_{\text{ac}} \cos(\omega t)) \quad (12)$$

with $\omega_{n,e}$ is the natural undamped resonance frequency in the presence of electrostatic spring softening, that is:

$$\omega_{n,e} = \sqrt{\frac{K_{\text{eff},e}}{M_{\text{eff}}}} = \sqrt{\frac{192 \frac{EI}{L_f^3} + 2.4 \frac{F_{\text{appl}}}{L_f} - \frac{\epsilon_0 h L_p}{g^3} V_{\text{dc}}^2 (1 + \alpha)}{\rho h \left(\frac{13}{35} w_f L_f + w_p L_p + w_c L_c \right)}}. \quad (13)$$

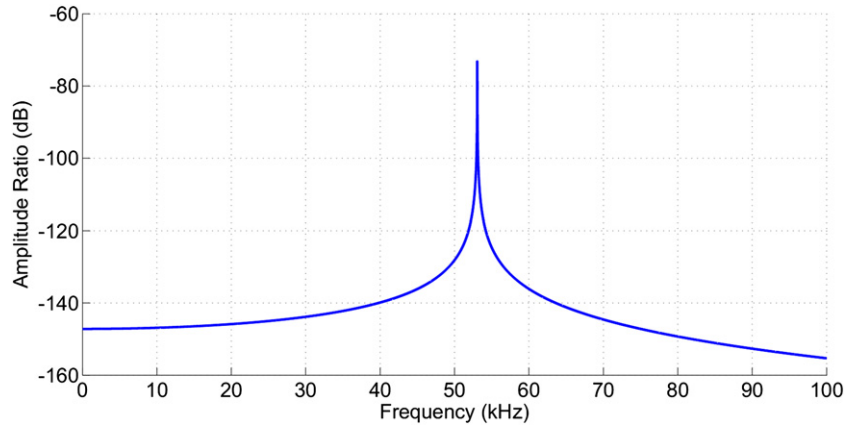


Figure 4. Simulated frequency response of the single tine.

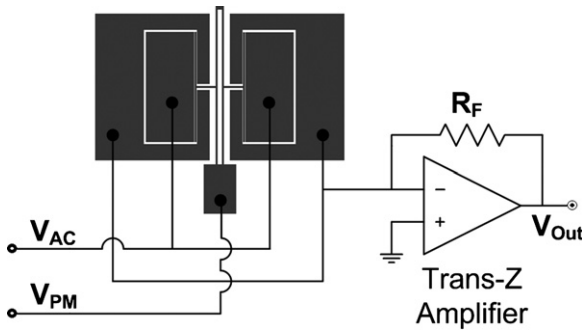


Figure 5. The complete DETF unit with connected ends and shorted drive and sense plates.

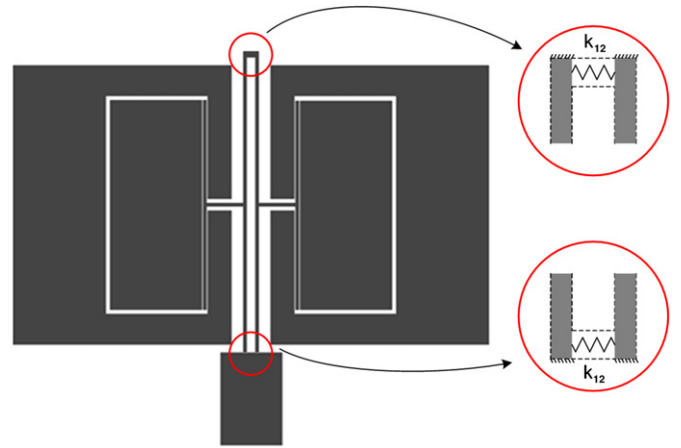


Figure 6. Coupling springs originating from non-rigid tine connections.

The motion of the tine induces a current proportional to its velocity, which can be sensed at the sensing plate and converted to a voltage signal via a trans-impedance amplifier of resistance R (figure 3):

$$V = \frac{R\epsilon_0 h L_p V_{dc}}{g^2} \dot{y}. \quad (14)$$

The variation of the output voltage amplitude V (normalized by V_{ac}) with forcing frequency (i.e., the frequency response of the tine) is depicted in figure 4.

2.2. A 2-DOF electromechanical lumped model

The analysis presented in section 2.1 assumes that no electromechanical coupling exists between the tines; this is tantamount to assuming perfectly rigid connecting pads. In a practical implementation, the complete DETF would be wired as indicated in figure 5. Obviously, the pads at the end of the tines have finite compliance. Structurally connecting the tines with a real (i.e., non-rigid) material results in an additional coupling spring (k_{12}) and an additional coupling damper (c_{12}) (figure 6).

The former arises due to the elastic deformation of the connecting region, whereas the latter represents the damping effect of the air between the tines.

The value of k_{12} can be readily estimated with the following consideration. If the middle point of one tine is

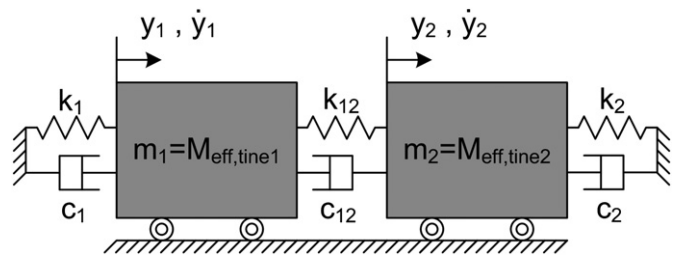


Figure 7. The lumped model of the DETF with tine coupling.

displaced transversely by an amount u_1 , the middle point of the second tine will tend to displace in the same direction by an amount u_2 . From dimensional analysis, u_2/u_1 can only depend on w_f/L_f and d/L_f , with w_f and L_f the width and length of the tine, respectively, and d the distance between the tines. From the lumped model of figure 7, it immediately follows that $K_{12}/K_1 = f/(1 - f)$, with $K_1 = K_{eff}$ the lumped stiffness of a tine (equation (11)) and $f = u_2/u_1$. f can be readily calculated by a finite element (FE) analysis. For the DETF sensor design in table 1, an FE analysis reveals $K_{12}/K_1 = 0.0017$. A fit on experimental measurements (see section 4) provides a coupling stiffness which is roughly two times

Table 1. Summary of geometric dimensions and electrical parameters of the DETF design for the response analysis. See figure 2 for variable definition.

Parameter	Symbol	Value (μm)
Tine length	L_f	964
Tine width	w_f	10
Capacitive plate length	L_p	680
Capacitive plate width	w_p	10
Capacitive gap	g	5
Connector length	L_c	120
Connector width	w_c	10
Device thickness	h	100
Proof mass voltage	V_{dc}	20 V
Trans- R feedback resistance	R	4.5 M Ω

higher, in acceptable agreement with the model; the difference is attributed to geometric imperfections. Note that for perfectly rigid connectors, $f = 0$ and hence $K_{12} = 0$. Although the value of c_{12} is negligibly small for vacuum operation, it could become significant under ambient conditions, and thus we will retain it in the derivation for completeness.

Modeling this electromechanical coupling requires at least a 2-DOF system analysis. Figure 7 depicts a schematic of the lumped model for a 2-tine DETF. The overall set of equations of the system can be written in the state-space representation as:

$$\begin{aligned} m_1 \ddot{y}_1 + c_1 \dot{y}_1 + c_{12}(\dot{y}_1 - \dot{y}_2) + k_1 y_1 + k_{12}(y_1 - y_2) &= P_{e,1} \\ m_2 \ddot{y}_2 + c_2 \dot{y}_2 + c_{12}(\dot{y}_2 - \dot{y}_1) + k_2 y_2 + k_{12}(y_2 - y_1) &= P_{e,2} \end{aligned} \quad (15)$$

where m_1 and m_2 are individual effective lumped masses (M_{eff}) of each tine, k_1 and k_2 are individual effective lumped spring constants ($K_{\text{eff},e}$) of each tine and c_1 and c_2 are the individual effective lumped damping coefficients acting on each tine. This system of equations can be expanded to include small fabrication variations of masses, spring constants and electromechanical parameters. Introducing these variations in equation (15) and replacing the mass term with the one in equation (6) and spring constant term with the one in equation (11) results in

$$\begin{aligned} [M_{\text{eff}}(1 + \varepsilon_{m1})] \ddot{y}_1 + c_1 \dot{y}_1 + c_{12}(\dot{y}_1 - \dot{y}_2) \\ + K_{\text{Tine1}} y_1 + k_{12}(y_1 - y_2) &= P_e(1 + \varepsilon_{e1}) \\ [M_{\text{eff}}(1 + \varepsilon_{m2})] \ddot{y}_2 + c_2 \dot{y}_2 + c_{12}(\dot{y}_2 - \dot{y}_1) \\ + K_{\text{Tine2}} y_2 + k_{12}(y_2 - y_1) &= P_e(1 + \varepsilon_{e2}) \end{aligned} \quad (16)$$

where

$$\begin{aligned} K_{\text{Tine1}} &= K_{0,\text{eff},e}(1 + \varepsilon_{k1}) + 2.4 \frac{F_{\text{appl}}}{L_f} (1 + \varepsilon_F) \\ K_{\text{Tine2}} &= K_{0,\text{eff},e}(1 + \varepsilon_{k2}) + 2.4 \frac{F_{\text{appl}}}{L_f} (1 - \varepsilon_F) \end{aligned} \quad (17)$$

and ε_m , ε_k , ε_e and ε_F are the variation coefficients for the mass, electromechanical spring constant, electromechanical transduction (electrostatic excitation and detection) and load sharing on each tine; these terms allow modeling of imperfections in all critical parameters. $K_{0,\text{eff},e}$ is the stiffness of the tine at zero applied force, that is

$$K_{0,\text{eff},e} = 192 \frac{EI}{L_f^3} - \frac{\varepsilon_0 h L_p V_{dc}^2}{g^3} (1 + \alpha). \quad (18)$$

Rewriting equation (16) in a matrix form to include the electromechanical excitation and detection terms yields

$$\begin{aligned} \dot{Y} &= AY + BU \\ V &= CY \end{aligned} \quad (19)$$

where V is the trans-impedance amplifier output voltage, U is the driving input voltage (in this case taken as equal to 1 V), and

$$Y = \begin{bmatrix} y_1 \\ \dot{y}_1 \\ y_2 \\ \dot{y}_2 \end{bmatrix} \quad (20)$$

$$A = \begin{bmatrix} 0 & 1 & 0 & 0 \\ -\left(\frac{K_{\text{Tine1}} + k_{12}}{M_{\text{eff}}(1 + \varepsilon_{m1})}\right) & -\left(\frac{c_1 + c_{12}}{M_{\text{eff}}(1 + \varepsilon_{m1})}\right) & \frac{k_{12}}{M_{\text{eff}}(1 + \varepsilon_{m1})} & \frac{c_{12}}{M_{\text{eff}}(1 + \varepsilon_{m1})} \\ 0 & 0 & 0 & 1 \\ \frac{k_{12}}{M_{\text{eff}}(1 + \varepsilon_{m2})} & \frac{c_{12}}{M_{\text{eff}}(1 + \varepsilon_{m2})} & -\left(\frac{K_{\text{Tine2}} + k_{12}}{M_{\text{eff}}(1 + \varepsilon_{m2})}\right) & -\left(\frac{c_2 + c_{12}}{M_{\text{eff}}(1 + \varepsilon_{m2})}\right) \end{bmatrix}, \quad (21)$$

$$B = \begin{bmatrix} 0 \\ -\frac{\varepsilon_0 h L_p V_{dc}}{g^2 M_{\text{eff}}(1 + \varepsilon_{m1})} (1 + \varepsilon_{e1}) \\ 0 \\ \frac{\varepsilon_0 h L_p V_{dc}}{g^2 M_{\text{eff}}(1 + \varepsilon_{m2})} (1 + \varepsilon_{e2}) \end{bmatrix} \quad (22)$$

and

$$C = \begin{bmatrix} 0 & \frac{R \varepsilon_0 h L_p V_{dc}}{g^2} (1 + \varepsilon_{e1}) & 0 & -\frac{R \varepsilon_0 h L_p V_{dc}}{g^2} (1 + \varepsilon_{e2}) \end{bmatrix} \quad (23)$$

A closed form solution for a system of this form is investigated in detail in [12]. There are two important aspects of the system: (i) the modal frequencies (eigenvalues of matrix A) and (ii) the mode shapes (i.e., the corresponding eigenvectors). The simplified (no damping) characteristic equation of A can be written in the form [12]

$$\omega^4 - \omega^2(\omega_a^2 + \omega_b^2) + (\omega_a^2 \omega_b^2 - \omega_{ab}^4) = 0 \quad (24)$$

where

$$\begin{aligned} \omega_a^2 &= \frac{K_{\text{Tine1}} + k_{12}}{M_{\text{eff}}(1 + \varepsilon_{m1})}, \\ \omega_b^2 &= \frac{K_{\text{Tine2}} + k_{12}}{M_{\text{eff}}(1 + \varepsilon_{m2})}, \\ \omega_{ab}^2 &= \frac{k_{12}}{M_{\text{eff}} \sqrt{(1 + \varepsilon_{m1})(1 + \varepsilon_{m2})}}. \end{aligned} \quad (25)$$

Here, ω_a is the system frequency when the second tine is clamped and ω_b is the system frequency when the first tine is clamped. ω_{ab} is a term related to the strength of the coupling. Equation (24) has two solutions, resulting in two frequency peaks:

$$\begin{aligned} \omega_1^2 &= \frac{(\omega_a^2 + \omega_b^2)}{2} - \sqrt{\left(\frac{(\omega_b^2 - \omega_a^2)}{2}\right)^2 + \omega_{ab}^4} \\ \omega_2^2 &= \frac{(\omega_a^2 + \omega_b^2)}{2} + \sqrt{\left(\frac{(\omega_b^2 - \omega_a^2)}{2}\right)^2 + \omega_{ab}^4}. \end{aligned} \quad (26)$$

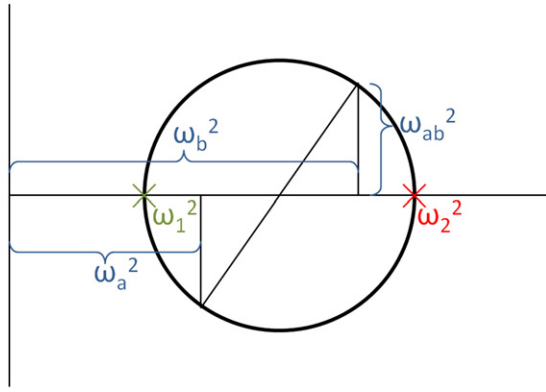


Figure 8. Mohr's circle relating ω_1 , ω_2 , ω_a , ω_b and ω_{ab} [12].

These two fundamental frequencies can be graphically depicted on Mohr's circle in figure 8 [12]. The lowest corresponds to the in-phase mode, whereas the latter represents the anti-phase mode.

For a perfectly symmetric DETF structure ($\varepsilon_m = \varepsilon_k = \varepsilon_e = \varepsilon_F = 0$) without any damping, the two modal frequencies simplify to

$$\begin{aligned} \omega_{1,p}^2 &= \frac{K_{\text{eff},e}}{M_{\text{eff}}} \\ \omega_{2,p}^2 &= \frac{K_{\text{eff},e} + 2k_{12}}{M_{\text{eff}}} \end{aligned} \quad (27)$$

Hence, the frequency separation at zero load is

$$\omega_{2,p} - \omega_{1,p} = \frac{\sqrt{K_{\text{eff},e} + 2k_{12}} - \sqrt{K_{\text{eff},e}}}{\sqrt{M_{\text{eff}}}} \quad (28)$$

As the compressive tip loading increases, the effective stiffness of the tines decreases (equation (11)). When the load reaches a critical value ($\omega_{1,p} = 0$) buckling occurs. The buckling load is

$$F_{\text{buckling},p} = \frac{-192 \frac{EI}{L_f^2} + \frac{\varepsilon_0 h L_f L_p}{g^3} V_{\text{dc}}^2 (1 + \alpha)}{2.4} \quad (29)$$

When the tine buckles, the frequency of the second mode, which is the minimum operational frequency for this mode, is

$$\omega_{2,\text{min},p} = \sqrt{\frac{2k_{12}}{M_{\text{eff}}}} \quad (30)$$

Equation (30) defines the lower frequency limit for the DETF operation, if second mode shape (out-of-phase) is chosen. This limit is defined by the buckling load for the first mode shape (in-phase mode). Obviously, in the ideal case of perfectly rigid connection between the tines ($k_{12} = 0$), the separation between the modes vanishes and we recover the results of the 1-DOF model.

Any asymmetry in the system (primarily caused by manufacturing imperfections) would affect the natural frequencies of the two modes, as shown in equation (26). The effect of these imperfections on the DETF response is discussed in the next section.

3. Effect of tine coupling and manufacturing imperfections

The impact of parameter variations (in mass, spring constant, electromechanical excitation-detection coefficients and load sharing of the tines) on the sensor response for a prototypical DETF resonator is analyzed. As the model presented in this paper reduces to the existing model (i.e., a single mass model with no geometric imperfections and perfectly symmetrical load distribution between the tines) when all asymmetries are set to zero, this section allows a quantitative comparison of the two formulations, providing motivation for the proposed development. A list of the geometric dimensions and electrical parameters assumed are given in table 1.

3.1. Imbalance in tines stiffness

Figure 9 provides a snapshot of the sensitivity of the frequency response of the DETF (design parameters in table 1) to small variations in the lumped effective spring constant of one of the tines, with all other parameters kept constant and equal for both tines.

The coupling stiffness k_{12} is also assumed to be zero to capture the effect of lumped spring constant variation of one tine. As expected, in the absence of asymmetries (i.e., when the tines have exactly the same values for all parameters), there is only a single peak. Increasing the tine stiffness imbalance results in the appearance of a second peak and an increasing separation of the modal frequencies. The minima in the amplitude/frequency curves emerge as a result of the interaction of the two tines, at a frequency where the phases are opposite and the amplitudes very close (destructive interference). Note that the zero-response frequency (the 'minimum amplitude' frequency) also shifts left with increasing tine stiffness imbalance.

3.2. Imbalance in tines mass

Figure 10 shows the dependence of the frequency response of the DETF (design parameters in table 1) to small variations in the lumped effective mass of one of the tines. Again, all other parameters (including the stiffness terms) are kept constant and equal for both tines. The effect is similar to that of stiffness imbalance (figure 9), with the exception that this time the peak is shifted in the opposite direction.

3.3. Effect of coupling stiffness from the end blocks

Introducing the coupling spring, k_{12} , induces a separation of the modal frequencies, as evident from the Mohr circle representation (figure 8) and equation (28). Figure 11 shows the frequency responses of the DETF with different coupling stiffness values, with a 1% tine stiffness imbalance. The 1% imbalance is introduced in order to make both peaks visible. As the peak progressively separate with increasing coupling, the zero-response point (which is unaffected by the numerator of the transfer function) does not move, while the lower frequency peak (corresponding to the in-phase mode) gets closer to the zero-response frequency and decreases in amplitude. This kind

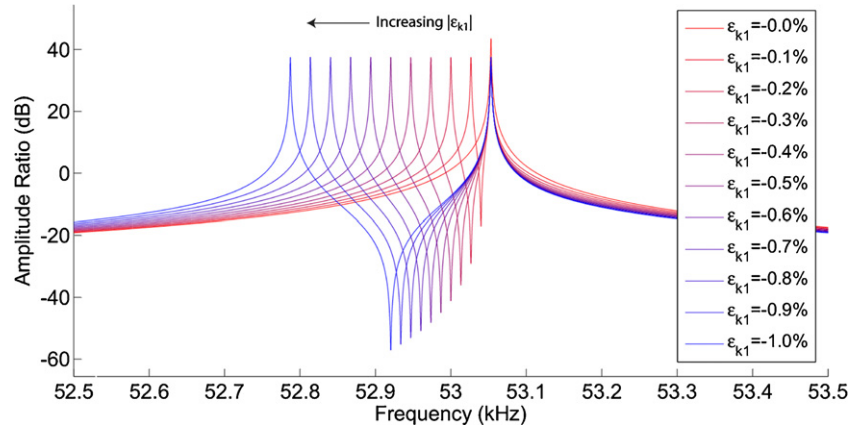


Figure 9. Effect of tine stiffness imbalance on the frequency response of the DETF (design parameters in table 1).

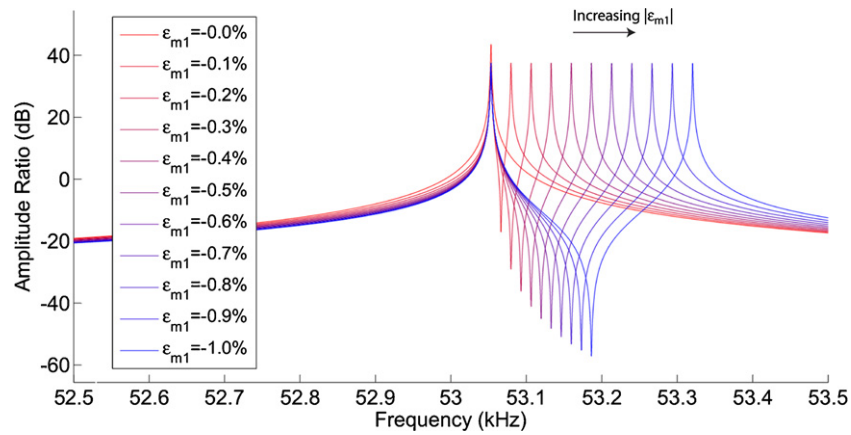


Figure 10. Effect of tine mass imbalance on the frequency response of the DETF (design parameters in table 1).

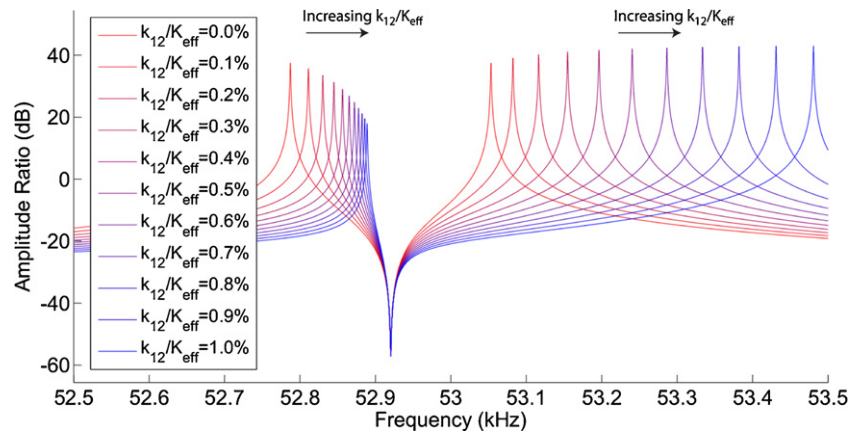


Figure 11. Effect of the coupling stiffness on the frequency response of the DETF, with a tine stiffness imbalance of 1% (design parameters in table 1).

of suppression is critical in the normal operation of the DETF because the control electronics should avoid locking to the lower frequency peak and jumping from one peak to the other, especially under larger load fluctuations.

3.4. Imbalance in electromechanical parameters

In addition to variations in the mechanical parameters discussed above, by virtue of the coupled nature of

MEMS capacitive structures, electromechanical parameters like voltage-to-force conversion coefficients (second and fourth terms in matrix B , equation (22)) and velocity-to-voltage conversion coefficients (second and fourth terms in matrix C , equation (23)) also affect the overall sensor response. Figure 12 shows the frequency response of the DETF with different electromechanical parameter variations, with a tine stiffness imbalance of 1%. Here, ϵ_{e1} is the variation in the term $\epsilon_0 h L_p V_{dc} / g^2$, which appears in both the B and C matrices.

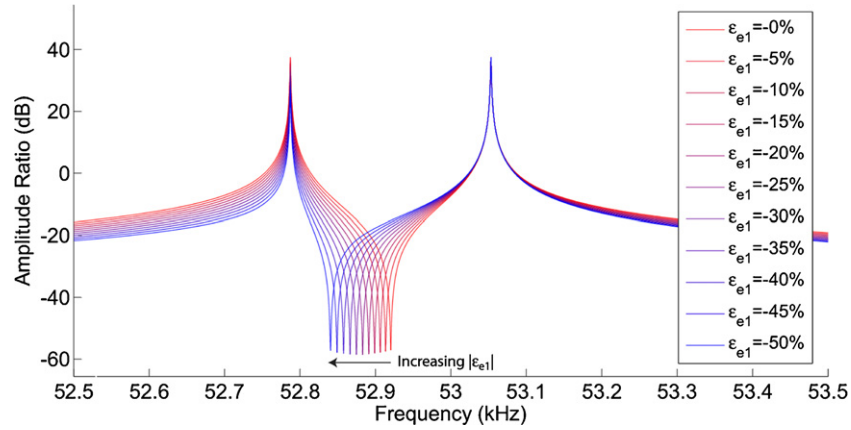


Figure 12. Effect of electromechanical parameter imbalance on the frequency response of the DETF (design parameters in table 1).

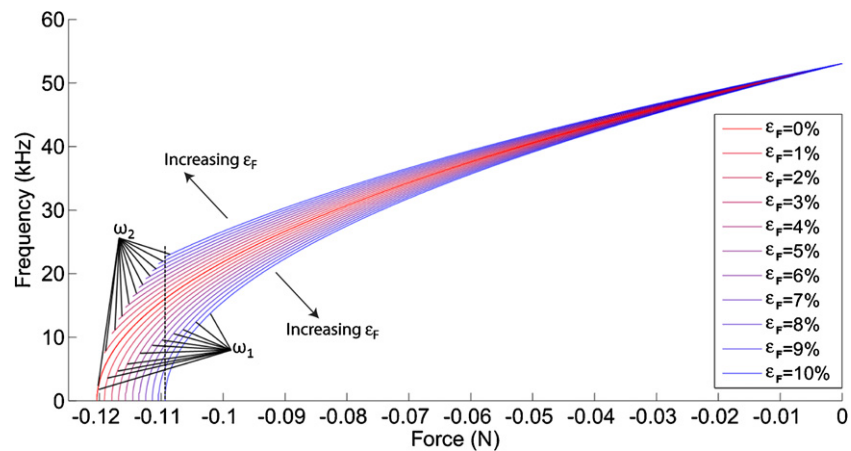


Figure 13. The evolution of the force–frequency relation of the DETF (design parameters in table 1) with respect to load imbalance, ϵ_F , on the tines, in the absence of coupling ($k_{12} = 0$). In the graph, the frequency gap between the first and the second resonant modes increases faster with increasing imbalance, and for each value of ϵ_F , the first mode hits zero-frequency (meaning pull-in, or buckling) well before the second mode, as indicated by the dashed vertical line.

Practically, these imbalances are induced by variations in two geometric parameters: the width of the capacitive gap, g , and the length of the capacitive plate, L_p . Importantly, the capacitive gap also affects the spring constant of the tines, i.e., any increase in the gap results in a decrease in tine width, resulting in a reduced mechanical tine stiffness; this effect is lumped in the parameter ϵ_{k1} in figure 9. Note that the electromechanical parameters hardly affect the ‘resonance frequencies’ or ‘frequencies of poles’ of the two modes, but they do affect the ‘frequency of the zero’ that emerges between the modes.

3.5. Load sharing between the tines

Beyond all the possible asymmetries discussed above, there is one more parameter that can be affected by fabrication imperfections: the load sharing between the tines. Although the structure is perfectly symmetric by design, any fabrication imperfection, causing slight cross-section variations in the tines, results in an imbalanced load distribution. This imbalance has profound effects on the dynamic range and the maximum operational loading of the sensor. Figure 13 shows the evolution of the force–frequency relation of the DETF

(design parameters in table 1) with respect to load imbalance, ϵ_F , on the tines, in the absence of stiffness coupling ($k_{12} = 0$). As is evidently shown in the graph, the frequency gap between the first and the second resonant modes increases faster with increasing imbalance, and the first mode hits zero-frequency (meaning pull-in, or buckling) well before the second mode.

Since stiffness coupling is ignored in figure 13, the plots for ω_1 and ω_2 are identical when $\epsilon_F = 0$. Upon the introduction of a coupling stiffness of 1% of the nominal tine stiffness ($k_{12} = k_1/100$), the frequency-force profiles for ω_1 and ω_2 at $\epsilon_F = 0$ separate, as shown in figure 14. Yet the relation between the gap of the modal resonance frequencies and the applied load as a function of load distribution between the tines is very similar to that of the zero-coupling case. Note that even for a small load imbalance ($\epsilon_F = 0.01$), the modes have a significant divergence: at a compressive force of ~ 120 mN, the in-phase peak falls below 0 Hz (signaling the onset of buckling), while the out-of-phase peak is still at ~ 9 KHz.

4. Experimental verification

As the asymmetries discussed in this model are induced by manufacturing imperfections and are impossible to eliminate

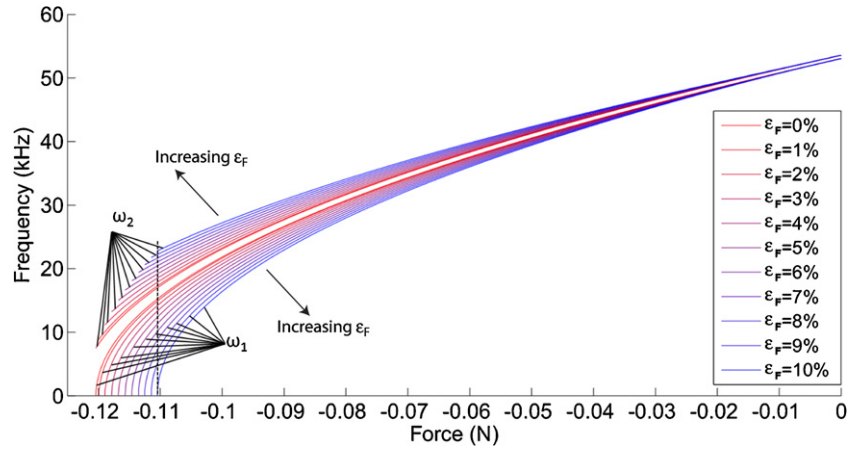


Figure 14. The evolution of the force–frequency relation of the DETF (design parameters in table 1) with respect to load imbalance, ϵ_F , on the tines, assuming a coupling stiffness of 1% of the tine stiffness ($k_{12} = k_1/100$). In the graph, the frequency gap between the first and the second resonant modes increases faster with increasing imbalance, and for each value of ϵ_F , the first mode hits zero-frequency (meaning pull-in, or buckling) well before the second mode, as indicated by the dashed vertical line.

and/or accurately control, an experimental platform where individual asymmetries are selectively introduced one at a time for model validation is impossible to implement. Obviously, artificially large individual geometric asymmetries could be intentionally introduced in the design (e.g., 10% width difference between the tines) in order to dwarf all other effects; however, their impact on the DETF performance would be too large to be meaningful. Consequently, the experimental validation of the model is conducted by measuring the dynamic response of a real design and demonstrating that an excellent fit is obtained with the proposed model, when reasonable magnitudes for all asymmetries are assumed. The DETF design used for the experimental validation is identical to that described in [8]. The nominal design parameters are reported in table 1. The test setup and the frequency response of the DETF at zero load are illustrated in figure 15. The frequency sweep is performed using a LF353 OpAmp trans-impedance stage with 4.5 M Ω feedback resistor, in vacuum (2.7 mTorr) and with a proof mass voltage, $V_{dc} = 40$ V.

The effect of the feed-through capacitance is eliminated by a feed-through cancellation method similar to that discussed in [13], but using a manually adjusted gain stage instead of an identical device in close proximity. This is achieved by feeding the drive signal with opposite phase to a very small capacitance between the inverting input of the trans-impedance stage and manually setting the amplitude to match the injected currents by the feedthrough path and the added capacitive path. (In [13], manual gain setting was unnecessary, as identical devices have identical feedthrough paths.) Due to balanced excitation, the gain difference between two modes is significant (>20 dB) and the quality factor of the operational mode is above 60 000. This guarantees locking on the desired mode. In theory, the in-phase mode can be eliminated entirely by perfectly symmetric driving (whereby the forcing signal on the two tines has no phase difference); in practice, any geometric or chip/substrate bonding asymmetry would make it appear, as discussed above. As the frequency separation of the two modes is very small (for the geometry under consideration, the measured in-phase mode has a natural frequency of 47.28 kHz versus a frequency

of 47.63 kHz for the out-of-phase mode), balanced actuation is crucial. It should also be noted that these are the first modes visible with balanced excitation and detection of the parallel plate structure, implying that the parasitic modes 1 and 2 in [8] are not interfering at zero load.

Based on the analysis in section 2.2, a fitting study is performed on the zero-axial load frequency response obtained in figure 15, resulting in the curve depicted in figure 16 with a coefficient of determination (R^2) of 95.4% (0.954). The imperfection parameters extracted from the fit are listed in table 2. Note that ϵ_{m1} and ϵ_{m2} are similar. The same applies to ϵ_{in1} and ϵ_{out1} , and to ϵ_{in2} and ϵ_{out2} also. There is a slight difference between ϵ_{k1} and ϵ_{k2} . Finally ϵ_{in1} is almost twice as large as ϵ_{in2} . These parameters are consistent with a fairly uniform undercut of the structure, possibly due to slight scaling effects during the pattern transfer steps and additional deep reactive ion etch.

To capture the effect of the load imbalance, a fitting study has been conducted on the loading test results reported in [8]. The loading test was conducted in a vacuum chamber with a viewport for alignment purposes. Figure 17 shows the test setup with Polytec MSA-500 white light interferometer for sample-to-sensor alignment. The sample is aligned to the sensor at atmospheric pressure via a 10-DOF stage (details in [8]), and the alignment is verified during the pump-down and loading stages to make sure that the force applied is aligned with the sensors' sensitive axis to the best extent possible. (Incidentally, this setup is capable of testing various thin film materials with the same precision.) The load is applied in compression, as this is the primary loading mode for micro-mechanical test frames (the key application for the proposed DETF design).

When the DETF is axially compressed, the experimental results show sudden buckling at a load much smaller than predicted with FEs simulations or analytical modeling (figure 18). The 2-DOF model presented in this work, with the same imbalance parameters fitted on the zero load response with a coefficient of determination (R^2) of 99.2% (0.992) (table 2) and a force imbalance, $\epsilon_F = 8.17\%$, captures the

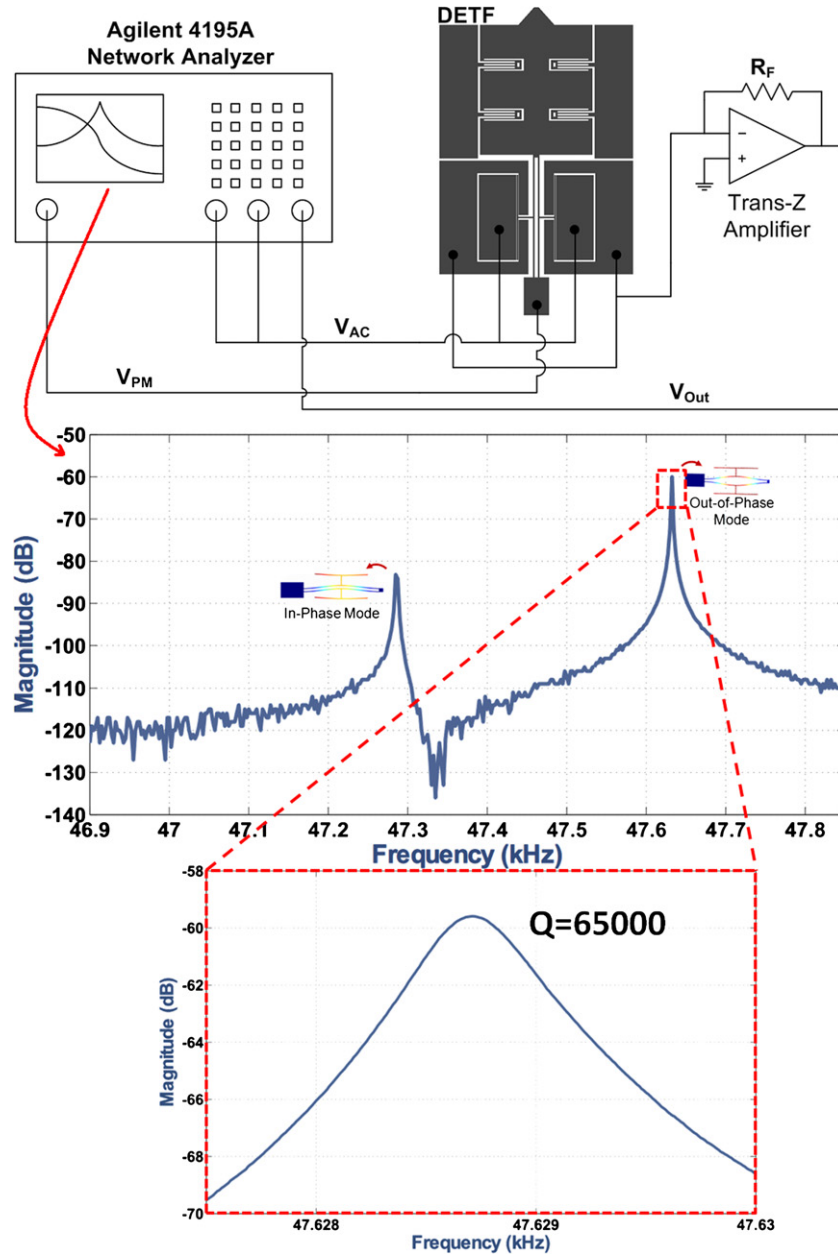


Figure 15. The test setup and the frequency response of the DETF at zero load.

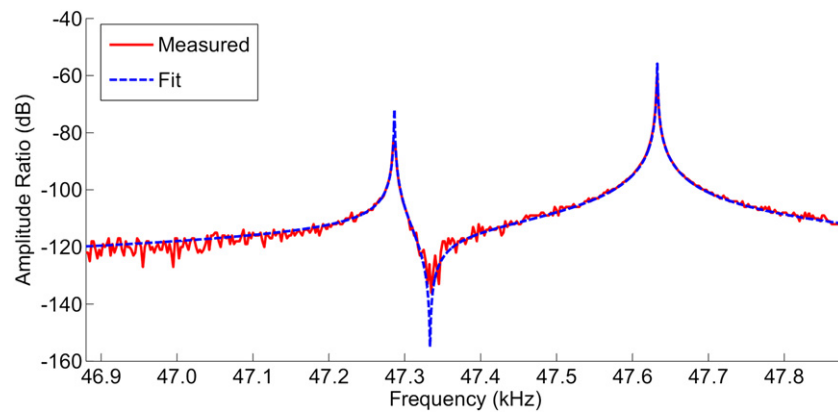


Figure 16. Fitting of the analytical 2-DOF model (equation (19)) on the experimental data depicted in figure 15 with a coefficient of determination (R^2) of 95.4% (0.954).

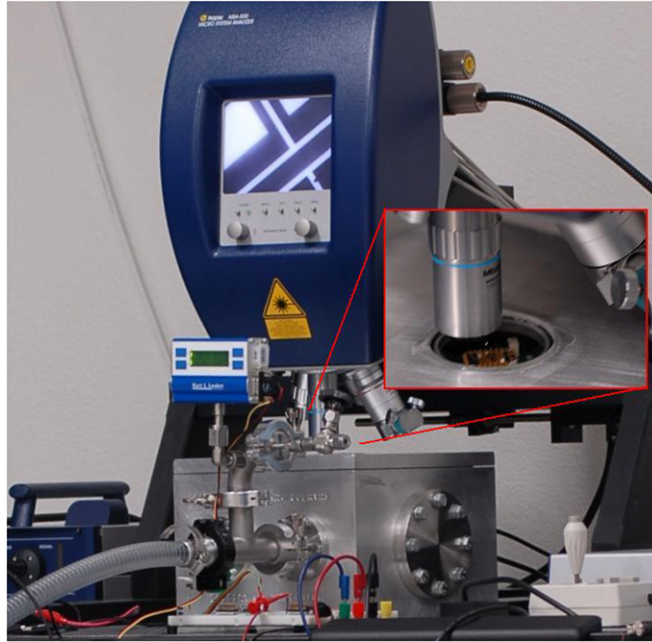


Figure 17. Vacuum test setup with Polytec MSA-500 white light interferometer for sample alignment.

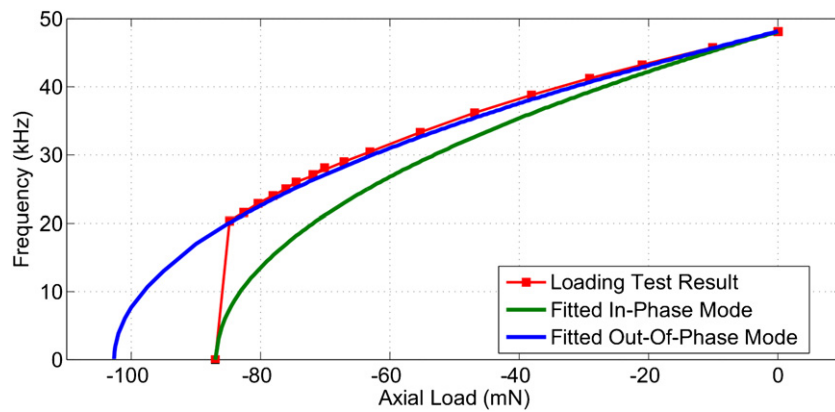


Figure 18. Fitting result of the analytical 2-DOF model (equation (19)) on the experimental loading test reported in [7]. The fitting, with a coefficient of determination (R^2) of 99.2% (0.992), assumes a force imbalance, $\epsilon_F = 8.17\%$, resulting in an early buckling of the in-phase mode, hence limiting the overall range of the force sensor.

Table 2. Fitted imperfection parameters.

ϵ_{m1}	ϵ_{m2}	ϵ_{k1}	ϵ_{k2}	ϵ_{in1}	ϵ_{in2}	ϵ_{out1}	ϵ_{out2}	k_{12} (N m^{-1})
-0.0313	-0.0313	-0.2154	-0.2248	-0.1144	-0.2739	-0.1144	-0.2739	0.9617

frequency/load trend for the out-of-plane mode as well as buckling of the in-phase mode in excellent agreement with the experimental results. By contrast, a single-DOF model, even fitted on the experimental results [8], overpredicts the buckling load by as much as 18%.

5. Conclusions

This paper presented a two-degree-of-freedom analytical model for the electromechanical response of double ended tuning fork (DETF) force sensors. The model captures the effect of the mechanical interaction between the tines and allows investigation of the effect of a number of asymmetries,

in tine stiffness, mass, electromechanical parameters and load sharing between the tines. The mechanical coupling between the tines (resulting from the finite stiffness of the tine connectors at both ends) induces a frequency separation between the in-phase and out-of-phase resonant modes. This separation cannot be captured by the standard single DOF model, and has profound implications on the electromechanical behavior of the sensor. The magnitude of the frequency separation and the relative intensity of the two peaks are affected by all the asymmetries mentioned above. To validate the model, a DETF sensor was designed and fabricated, and driven by a custom-built PLL circuit. The peak separation clearly emerged and the model presented

in this paper provided an excellent fit to the experimental frequency response, assuming reasonable values for all the geometric asymmetries. Two key conclusions can be extracted by this model: (i) as the external axial load is increased, the in-phase mode reaches zero frequency (buckling) much faster than the out-of-phase (i.e., operational) mode, effectively limiting the range of the device. This is consistent with previously published results [8]. (ii) During the operation, balanced excitation is essential to guarantee that the out-of-phase mode remain significantly stronger than the in-phase mode, thus allowing sharp PLL locking and hence robust performance. The proposed analytical model can be used to assess the magnitude of asymmetries introduced by a given manufacturing process and, more importantly, to accurately predict the performance of a DETF device in a real design.

Acknowledgments

The authors acknowledge partial funding from the Defense Advanced Research Projects Agency under the Materials with Controlled Microstructural Architecture program managed by J Goldwasser (contract no. W91CRB-10-0305) and by the California-Catalonia Program for Engineering Innovation.

References

- [1] Valdevit L, Jacobsen A J, Greer J R and Carter W B 2011 Protocols for the optimal design of multi-functional cellular structures: from hypersonics to micro-architected materials *J. Am. Ceram. Soc.* **94** 15–34
- [2] Blom F R, Bouwstra S, Fluitman J H J and Elwenspoek M 1989 Resonating silicon beam force sensor *Sensors Actuators* **17** 513–19
- [3] Cheshmehdoost A, Jones B E and O'Connor B 1991 Characteristics of a force transducer incorporating a mechanical DETF resonator *Sensors Actuators A* **26** 307–12
- [4] Howe R T, Boser B E and Pisano A P 1996 Polysilicon integrated microsystems: technologies and applications *Sensors Actuators A* **56** 167–77
- [5] Tilmans H A C, Elwenspoek M and Fluitman J H J 1992 Micro resonant force gauges *Sensors Actuators A* **30** 35–53
- [6] Vanmullem C J, Tilmans H A C, Mouthaan A J and Fluitman J H J 1992 Electrical cross-talk in 2-port resonators—the resonant silicon beam force sensor *Sensors Actuators A* **31** 168–73
- [7] Azgin K, Ro C, Torrents A, Akin T and Valdevit L 2011 A resonant tuning fork force sensor with unprecedented combination of resolution and range *MEMS'11: IEEE 24th Int. Conf. on Micro Electro Mechanical Systems* pp 545–48
- [8] Azgin K, Akin T and Valdevit L 2012 Ultrahigh-dynamic-range resonant MEMS load cells for micromechanical test frames *J. Microelectromech. Syst.* **99** 1–11
- [9] Torrents A, Azgin K, Godfrey S, Topalli E, Akin T and Valdevit L 2010 MEMS resonant load cells for micro-mechanical test frames: feasibility study and optimal design *J. Micromech. Microeng.* **20** 125004
- [10] Roessig T A W 1998 Integrated MEMS tuning fork oscillators for sensor applications *PhD Thesis* University of California, Berkeley p 137
- [11] Seshia A A 2002 Integrated micromechanical resonant sensors for inertial measurement systems *PhD Thesis* University of California, Berkeley p 140
- [12] Den Hartog J P 1985 *Mechanical Vibrations* (New York: Dover)
- [13] Lee J E Y and Seshia A A 2009 Parasitic feedthrough cancellation techniques for enhanced electrical characterization of electrostatic microresonators *Sensors Actuators A* **156** 36–42